A general framework for wave separation in the frequency domain

Enrique M. Padilla[a,*], José M. Alsina[b]

[a] *Department of Civil and Environmental Engineering, Imperial College of Medicine, Science and Technology, London, UK.*
[b] *Laboratori d'Enginyeria Marítima, Universitat Politecnica de Catalunya, C. Jordi Girona, 1-3 08034 Barcelona, Spain.*

Abstract

A general framework for wave separation in the frequency domain is presented and evaluated with successful results using theoretical examples of nonlinear waves. This framework consists of a qualitative and a quantitative analysis. The qualitative analysis is a novel approach that provides useful information about the existing wave trains within a wave field. This information includes an estimation of the number of wave trains, their direction of propagation (seaward or shoreward), their nature (free or bound) and their relative importance. The quantitative analysis consists in a revisited wave separation method applicable to separate free and bound wave trains travelling seaward and shoreward for both high and low frequencies propagating over uneven bathymetries. This versatility represents an improvement compared to existing methods. The presented separation method is low-sensitive to noise and its robustness is tested for a range of wave separation settings. The potential application of the separation method to random waves is discussed.

Keywords: Wave Separation, Wave Undulations, Nodes-Antinodes, Wave Interference, Wave-trains Superposition

*Corresponding author
Email addresses: e.padilla14@imperial.ac.uk (Enrique M. Padilla), jose.alsina@upc.edu (José M. Alsina)

1. Introduction

The water surface elevation is formed by a number of individual wave trains of very different characteristics (i.e., ingoing, outgoing, free, bound) operating at different frequencies. Therefore, the wave separation of water surface elevation signals into individual wave trains is a relatively common process when analysing field or laboratory data and numerical simulations.

Considering a cross-shore projection of the wave field, wave trains travelling towards the shoreline (ingoing) may coexist with wave trains travelling seawards (outgoing). For primary frequencies, the incident wave train is an Ingoing Free Wave (IFW). This free wave travels with the wave celerity given by the dispersion relationship. For superharmonics or subharmonics of the primary frequencies, the incident wave train is an Ingoing Bound Wave (IBW). This bound wave is the quadratic difference interaction of a pair of primary waves. Consequently, this bound wave travels with the wave structure of the primary waves (Biésel, 1952; Longuet-Higgins and Stewart, 1962). Wave trains travelling seawards are usually Outgoing Free Waves (OFW) caused by the reflection or radiation of waves generally occurring landward the surf zone. In sloping beaches, OFW become more important at low frequencies. For low frequencies, the reflection coefficients are typically large as observed by Elgar et al. (1994); Baquerizo et al. (1997); Van Dongeren et al. (2007). For high frequencies, the reflection coefficients are typically low and most of the energy content of the incident primary waves is dissipated at the surf zone (Elgar et al., 1994). Consequently, the existence of an Outgoing Bound Wave (OBW) at superharmonics or subharmonics of the primary frequencies is usually negligible (Kostense, 1985; Battjes et al., 2004; Van Dongeren et al., 2007).

More than one wave train propagating with the same frequency, but different celerities, give rise to a clear undulating pattern of the spatial envelope. The classical example of these spatial undulations is the envelope of the well known *standing waves*, where two waves of the same frequency and amplitude propagate in opposite direction. Similar undulating patterns may also be identified within

a variety of wave fields under different combinations of IBW, OBW, IFW and OFW. For low frequencies, spatial undulations due to the combination [IBW, OFW] are observed at the group frequency in Baldock et al. (2000) (Figures 9-12), Alsina and Cáceres (2011) (Figure 5), Alsina et al. (2016) (Figures 10-11) and Padilla and Alsina (2017) (Figure 9). Spatial undulations due to the combination [IBW, IFW, OFW] are seen in Padilla and Alsina (2018) (Figures 5-6) when a moving breakpoint radiates long waves both seaward and shoreward. Symonds et al. (1982) proposed this moving breakpoint mechanism, whereas Padilla and Alsina (2018) analysed the associated spatial undulating patterns within the surf zone and outside the surf zone. Within the surf zone, an undulating pattern related to [IBW, IFW, OFW] is observed. Outside the surf zone, a different undulating pattern related to the pair [IBW, OFW] is observed. For high frequencies, spatial undulations may appear at primary frequencies and superharmonics of primary frequencies, as seen by Goda and Suzuki (1976) (Figure 8). However, spatial undulations at high frequencies have tradiationally received less attention than spatial undulations at low frequencies.

Different wave separation methods where only measurements of the water surface elevation are used have been presented during the last decades, e.g., Goda and Suzuki (1976); Mansard and Funke (1980); Kostense (1985); Frigaard and Brorsen (1995); Baldock and Simmonds (1999); Suh et al. (2001); Lin and Huang (2004); Battjes et al. (2004); Van Dongeren et al. (2007); Andersen et al. (2017). The aim of these methods is the distribution of the wave energy budget into potential wave trains. To do so, these methods account for the relative differences in the spatial evolution of those wave trains during their propagation. Some of the above mentioned methods are applied in the time domain, e.g., Frigaard and Brorsen (1995) and Baldock and Simmonds (1999), whereas most of the existing methods are applied in the frequency domain. The basis of the methods applied in the frequency domain was developed by Thornton and Calhoun (1972) and Goda and Suzuki (1976), where incident and reflected waves were computed from two locations in line with the direction of wave propagation. This preliminary version (called *The 2-point Method*)

was built upon monochromatic waves, but it was highly sensitive to noise and had serious limitations related to the frequency range, which depends on the spacing between the probes. The 2-point Method was improved by Mansard and Funke (1980) increasing the number of probes from two to three and reducing the sensitivity to noise by including the least square method. However, further improvements came with Zelt and Skjelbreia (1993) and Baquerizo (1995). Zelt and Skjelbreia (1993) proposed the increase in the number of probes from three to a larger and arbitrary number. This increase is currently common practice in a number of methods, e.g., Battjes et al. (2004), Lin and Huang (2004), Van Dongeren et al. (2007) or Andersen et al. (2017), among others. Baquerizo (1995) provided a more solid mathematical background to the separation method proposed by Mansard and Funke (1980). Since then, much effort has been done in order to adapt the separating methods to the target wave field. For low frequencies, Kostense (1985) adapted the separation method to include group-bound incident waves propagating on a flat bed. Battjes et al. (2004) and Van Dongeren et al. (2007) extended the separation of incident bound waves and outgoing free waves over an sloping bed. For high frequencies, the separation method proposed by Lin and Huang (2004) and Andersen et al. (2017) provides satisfactory results limited to flat beds. Particular effects like amplitude dispersion or the existence of a known current are only considered in Andersen et al. (2017) and Suh et al. (2001), respectively.

The fact that there is not a single wave separation method, but a variety of them, indicates a generalized lack of versatility. These methods provide satisfactory outcomes only for the wave fields they were designed for. Therefore, selecting the suitable separation method for the target wave condition becomes significantly important. Moreover, even having the wave separation done, being able to analyse if the outcomes from the wave separation are physically consistent is also important. Unfortunately, a qualitative analysis to identify certain hints of the existing wave trains from the observed spatial undulating patterns does not exist yet.

This paper aims to provide a new general framework for wave separation in

the frequency domain. The framework consists of a qualitative and quantitative analysis. The qualitative analysis is a new approach based on the observation of the undulating patterns of the cross-shore wave amplitude at the target frequency. This qualitative analysis estimates the number of existing wave trains, their nature and their relative importance before applying the quantitative analysis. The quantitative analysis consists in a highly-versatile wave separation method in the frequency domain. This framework for wave separation has already been applied to laboratory conditions (Alsina et al., 2016; Padilla and Alsina, 2017, 2018), but can be also applied to numerical simulations or field data having a minimal spatial resolution. This paper is organized as follows. Section 2 presents the qualitative analysis. Section 3 presents the quantitative analysis. Section 4 shows the validity of this general framework for wave separation on theoretical wave cases with satisfactory results. Section 5 discusses the qualitative and quantitative analyses alongside with the sensitivity to white noise and robustness of the method. The potential application of the separation method to random waves is also discussed. Finally, the conclusions are presented in section 6.

2. Qualitative analysis

2.1. Spatial undulations of the wave envelope

The superposition of different wave trains has direct observable effects on the resultant surface elevation. When two wave crests meet at the same time-space, they are in phase and the resulting crest is the linear sum of the individual crests. In this case, their interference is constructive (see Figure 1a). When a wave crest and a wave trough meet at the same space-time, the two features are in antiphase and they cancel out (if their amplitudes are the same). In this case, their interference is destructive (see Figure 1b). Therefore, the sequence of constructive and destructive interferences is a common process between propagating wave trains with different celerities or different propagation direction.

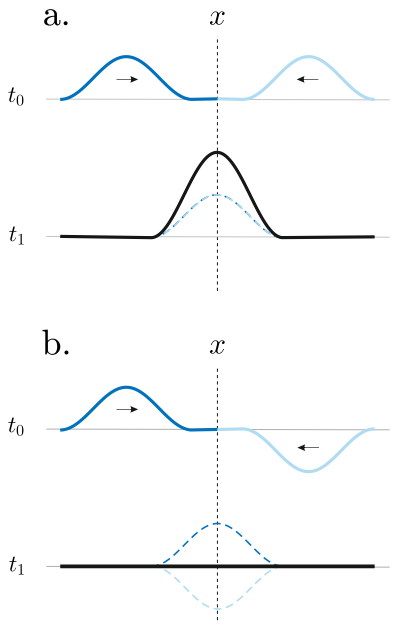

Figure 1: Sketch of constructive (plot *a*) and destructive (plot *b*) wave interferences.

When two wave trains propagate with the same frequency but different celerities, the spatial distribution of their relative phases is stationary, i.e., the wave field η varies in time beneath a spatial envelope $|\hat{\eta}|$ that remains constant. In particular, the linear superposition of two wave trains with the same wave amplitude (i.e., $A_1 = A_2 = A$) and propagating in opposite direction with the same celerity give rise the well known *standing wave* pattern (Figure 2a). At locations where the wave trains are in phase (constructive interference), the vertical motion of a water particle is maximum ($A_1 + A_2 = 2A$). At locations where the wave trains are in antiphase (destructive interference), the vertical motion is null ($A_1 - A_2 = 0$). Therefore, the spatial envelope $|\hat{\eta}|$ presents an undulation (see Figure 2a) where the locations with maximum and null vertical motion are called antinodes and nodes, respectively. Furthermore, the fact that the wave trains travel in opposite direction suppresses any spatial motion of the total superposed wave motion. When $A_1 \neq A_2$ the resulting wave field is no longer a standing wave. The minimal vertical elevation is now $|A_1 - A_2| \neq 0$

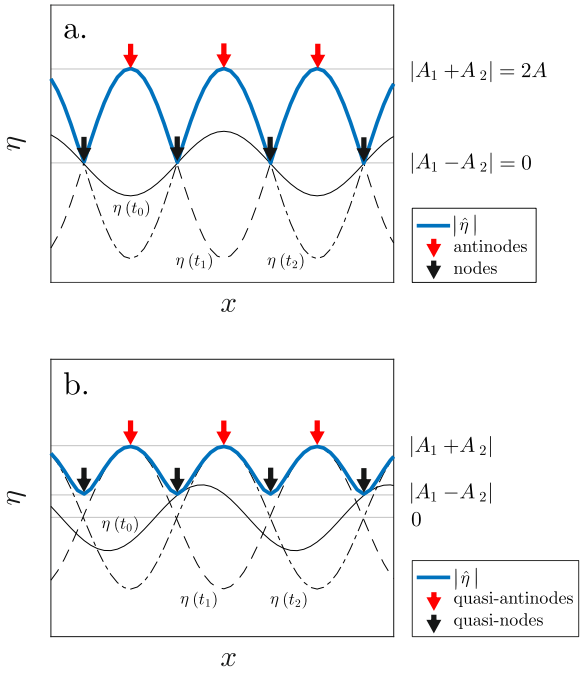

Figure 2: Sketch of the wave field η at three different time instants and their spatial envelope $|\hat{\eta}|$ for wave trains with the same amplitude ($A_1 = A_2$ in plot *a*) and different amplitude ($A_1 \neq A_2$ in plot *b*). Plot *a* shows a standing wave pattern where the spatial undulation of $|\hat{\eta}|$ is formed of nodes and antinodes, whereas the undulation of $|\hat{\eta}|$ in plot *b* is formed of quasi-nodes and -antinodes.

and the spatial envelope $|\hat{\eta}|$ presents an undulation formed of quasi-nodes and quasi-antinodes (see Figure 2b). As a result, there is a progressive wave motion in the direction of the dominant wave train. In general, when $A_1 \neq A_2$ and the wave trains propagate with different celerities, the spatial envelope presents an undulation with quasi-antinodes and quasi-nodes.

Note that the "node-antinode" notation should only be applied to standing waves. However, henceforth, the locations where two wave trains are in phase will be called *antinodes*. The locations where two wave trains are in antiphase will be called *nodes*.

2.2. Nodes and antinodes in pairs of wave trains

The spatial envelope of two wave trains with the same frequency but different propagation characteristics (celerities) always displays one undulating pattern consisting of nodes and antinodes. Therefore, the simultaneous propagation of n different wave trains will develop N different node-antinode patterns, whose expression:

$$N = \frac{n!}{2!(n-2)!}, \tag{1}$$

accounts for the number of combinations of unordered subsets of two wave trains within a certain set of n propagating wave trains. For instance, the spatial envelope of three different wave trains displays three different cross-shore node-antinode patterns, whereas the spatial envelope of five different wave trains displays ten different node-antinode patterns. Instead of analysing all the node-antinode patterns in one, a practical approach for the purpose of this paper is to individually analyse the resulting node-antinode pattern of pairs of wave trains.

In the following subsections, the location of a set of nodes and antinodes belonging to a pair of wave trains is analytically solved in the x-y space. The problem is addressed first for a flat bed ($h = const$) using linear wave theory. The analytical solution is then extended to a pair of wave trains propagating over changing water depths in the cross-shore direction ($h = h(x)$).

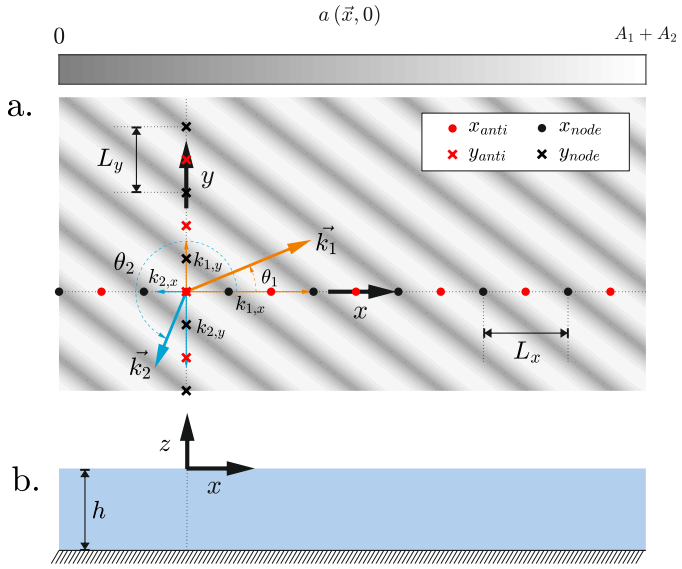

Figure 3: Sketch of the geometry for flat bed. Plot a shows the resultant envelope, $a(\vec{x},0)$, of the superposition of two wave trains travelling in the direction of their respective wave number vectors ($\vec{k_1}$ in orange, $\vec{k_2}$ in blue). The locations of the antinodes and nodes at the x-axis are $[x_{anti},\, x_{node}]$, whereas the locations of the antinodes and nodes at the y-axis are $[y_{anti},\, y_{node}]$. L_x and L_y are the distances between consecutive nodes (or antinodes) in the x and y axes, respectively. Plot b shows the cross-shore bathymetry $h = const.$

2.2.1. Flat bed

Figure 3 shows the general situation of two wave trains in the x-y space, whose angular frequency is ω, propagating in the direction of their respective wave number vectors $[\vec{k_1},\ \vec{k_2}]$ over a flat bed ($h = const$). For each wave train, if θ is the angle of incidence, defined as the angle between the x-axis and the wave-train direction, then $k_x = |\vec{k}|\,\cos(\theta)$ and $k_y = |\vec{k}|\,\sin(\theta)$ (See Figure 3). The resultant potential is

$$\phi(\vec{x},z,t) = \Re\left\{-i\frac{g}{\omega}\left(A_1\,K_{p,1}(z)\,e^{-i(\omega t-\vec{k_1}\,\vec{x}+\psi_1)} + A_2\,K_{p,2}(z)\,e^{-i(\omega t-\vec{k_2}\,\vec{x}+\psi_2)}\right)\right\}, \tag{2}$$

where $[A_1,\ A_2]$ are the respective wave amplitudes, $[\psi_1,\ \psi_2]$ are the respective initial phases, $K_p(z) = \cosh(k(z+h))/\cosh(k\,h)$ with $k = |\vec{k}|$, g is the gravitorial acceleration and i is the imaginary unit. Equation (2) may be rewritten in terms of the functions $a(\vec{x},z)$ and $\varphi(\vec{x})$ as

$$\phi(\vec{x},z,t) = \Re\left\{-i\frac{g}{\omega}\,a(\vec{x},z)\,e^{-i(\omega\,t+\varphi(\vec{x}))}\right\}, \tag{3}$$

whose resulting surface elevation is

$$\begin{aligned}\eta(\vec{x},t) &= -\frac{1}{g}\left.\frac{\partial\phi}{\partial t}\right|_{z=0}\\ &= a(\vec{x},0)\,\cos\left(\omega t+\varphi(\vec{x})\right).\end{aligned} \tag{4}$$

From Equation (4), $a(\vec{x},0)$ is the envelope of the surface elevation. Using the identity $e^{i\alpha} = \cos(\alpha) + i\sin(\alpha)$, where α is a convenient variable, the expression of the envelope $a(\vec{x},0)$ that satisfies Equation (3) is

$$\begin{aligned}\left[a\left(\vec{x},0\right)\right]^2 &= \left[A_1\,\cos\left(-\vec{k_1}\,\vec{x}+\psi_1\right) + A_2\,\cos\left(-\vec{k_2}\,\vec{x}+\psi_2\right)\right]^2\\ &+ \left[A_1\,\sin\left(-\vec{k_1}\,\vec{x}+\psi_1\right) + A_2\,\sin\left(-\vec{k_2}\,\vec{x}+\psi_2\right)\right]^2\\ &= {A_1}^2 + {A_2}^2 + 2\,A_1\,A_2\,\cos\left(-(\vec{k_1}-\vec{k_2})\,\vec{x}+(\psi_1-\psi_2)\right).\end{aligned} \tag{5}$$

By definition, $a(\vec{x},0)$ is maximum at the antinodes, whereas $a(\vec{x},0)$ is minimal at the nodes. Based on Equation (5), $a(\vec{x},0)$ is maximum and minimal when

$\cos\left(-(\vec{k_1}-\vec{k_2})\,\vec{x}+(\psi_1-\psi_2)\right)=\pm 1$, respectively. Therefore, the spatial locations of the antinodes are given by the following families of curves:

$$-\left(k_{1,x}-k_{2,x}\right)\,x-\left(k_{1,y}-k_{2,y}\right)\,y=2\pi m-(\psi_1-\psi_2)\quad\text{with } m\in\mathbb{Z}, \tag{6}$$

whereas for nodes:

$$-\left(k_{1,x}-k_{2,x}\right)\,x-\left(k_{1,y}-k_{2,y}\right)\,y=\pi(2m+1)-(\psi_1-\psi_2)\quad\text{with } m\in\mathbb{Z}. \tag{7}$$

Using Equations (6) and (7), the locations of the antinodes and nodes at the x-axis, i.e., $y=0$ (see Figure 3), are respectively:

$$x_{anti} = \frac{2\pi m-(\psi_1-\psi_2)}{-\left(k_{1,x}-k_{2,x}\right)}\quad\text{with } m\in\mathbb{Z}, \tag{8}$$

$$x_{node} = \frac{\pi(2m+1)-(\psi_1-\psi_2)}{-\left(k_{1,x}-k_{2,x}\right)}\quad\text{with } m\in\mathbb{Z}, \tag{9}$$

whose distance between consecutive antinodes L_x (identical distance between consecutive nodes) is

$$(L_x)^2=\left(\frac{2\pi}{-\left(k_{1,x}-k_{2,x}\right)}\right)^2. \tag{10}$$

Note that, in general, the distance between consecutive antinodes (or nodes) over flat beds does not depend on the amplitude of the involved wave trains, but depends on their propagation characteristics only, i.e., their wave numbers. Furthermore, according to Equations (8) and (9), the observation of the undulation resultant of the linear superposition of two wave trains over a flat bed provides information of their wave phases and wave numbers. Likewise, similar expressions for y_{anti} and y_{node} at the y-axis may be obtained, whose distance between consecutive antinodes (or nodes) is L_y (See Figure 3).

2.2.2. Changing water depths

The immediate effect of wave trains propagating on a sloping bed is the progressive reduction of their phase velocity as the water depth reduces. Therefore, the celerity of propagating wave trains changes as a function of the bathymetry. As a consequence, a wave train not propagating normal to the shoreline undergoes

refraction, i.e., the differential celerity along the wave front makes the angle of incidence θ to progressively reduce and the wave train tends to propagate normal to the shoreline. In particular, considering a bathymetry where $h = h(x)$, being the x-axis normal to the beach, a wave train with initial celerity c_0 and initial angle of incidence θ_0 describes a curvilinear trajectory $\theta(x)$ during its shoreward propagation due to a progressively changing wave number vector. The components of the average wave number ($\widetilde{k}_x$ and $\widetilde{k}_y$) accounting for the time required for a wave train with celerity $c(x)$ to travel a certain cross-shore distance x are:

$$\widetilde{k}_x(x) = \begin{cases} \frac{\omega}{c_0}\cos(\theta_0) & \text{if } x = 0, \\ \frac{\omega}{x}\int_0^x \frac{1}{c(x)}\cos(\theta(x))\,dx, & \text{if } x > 0, \end{cases} \tag{11}$$

$$\widetilde{k}_y(x) = \frac{\omega}{c(x)}\sin(\theta(x)) = const, \tag{12}$$

where the cross-shore evolution of the angle of incidence, $\theta(x)$, is given by Equation (12), which is the Snell's law.

For changing water depths in the way $h = h(x)$, Equations (6) and (7) still apply on defining the location of the nodes and antinodes if the cross-shore evolution of the wave number vectors is accounted, i.e., $k_x = \widetilde{k}_x(x)$ and $k_y = \widetilde{k}_y(x)$. As a result, the following implicit expressions are a generalization of Equations (8) and (9), respectively:

$$\int_0^{x_{anti}} \left(\frac{\cos(\theta_1(x))}{c_1(x)} - \frac{\cos(\theta_2(x))}{c_2(x)}\right) dx = -\frac{2\pi m - (\psi_1 - \psi_2)}{\omega} \quad \text{with } m \in \mathbb{Z}, \tag{13}$$

$$\int_0^{x_{node}} \left(\frac{\cos(\theta_1(x))}{c_1(x)} - \frac{\cos(\theta_2(x))}{c_2(x)}\right) dx = -\frac{\pi(2m+1) - (\psi_1 - \psi_2)}{\omega} \quad \text{with } m \in \mathbb{Z}, \tag{14}$$

where x_{anti} and x_{node} are the location of the antinodes and nodes at the x-axis ($y = 0$) when $h = h(x)$. Likewise, similar expressions for y_{anti} and y_{node} at the y-axis ($x = 0$) on changing water depths may be obtained (not showed).

2.3. Scheme of the qualitative analysis

The following steps summarize the qualitative analysis applied to a stationary signal at the target frequency. These steps provide information about the

number of existing wave trains, their propagation nature (free or bound), their ingoing or outgoing nature and their relative importance:

1. *Computation of the number of wave trains* (n). Given water surface elevation time series at different cross-shore locations with enough resolution (commented below), N is the number of existing node-antinode patterns within the cross-shore wave amplitude. N^* is the number of node-antinode patterns that an observer may identify within that cross-shore wave amplitude. The difference between N and N^* will be clearly seen below in Figure 7 and explained with more detail in Section 4.1.2. In Figure 7, only two clear node-antinode patterns are identified ($N^* = 2$), whereas three node-antinode patterns actually exist ($N = 3$). Therefore, if an observer identifies exactly N different node-antinodes patters ($N^* = N$), then, using Equation (1), the number n of existing wave trains is the positive solution of the equation $n^2 - n - 2N = 0$, i.e.,

$$n = \frac{1 + \sqrt{1 + 8N}}{2}. \tag{15}$$

   However, since $N^* \leq N$ in practice, the number of existing wave trains n based on the observation of N^* different node-antinode patterns is

$$n \geq \lceil 0.5\,(1 + \sqrt{1 + 8N^*}) \rceil, \tag{16}$$

   where the operator $\lceil \cdot \rceil$ rounds the element to the nearest higher integer.

2. *Identification of the free or bound nature of the wave trains and their propagation direction.* Two wave trains can propagate in the same direction or in opposite direction to each other. Therefore, assuming the relatively common combination [IBW, IFW, OFW], the following pairs may exist at the target frequency: [IFW, OFW], [IBW, IFW], [IBW, OFW]. Each of the previous pairs builds a node-antinode pattern and, therefore, identifying which of the above pairs is responsible for a certain undulating pattern may be achieved using Equations (13) and (14), or just using Equation (10) as a valid approximation of the mean distance between consecutive antinodes for each existing undulating pattern.

3. *Relative importance of the wave trains.* Assuming the relatively common combination [IBW, IFW, OFW], the overall trajectory of the surface elevation crests at the target frequency in the time-space contour plot matches with the trajectory of the dominant wave train. For instance, if IBW is observed to be the dominant wave train, then the relative importance between the remaining wave trains (IFW and OFW) is given by the relative amplitude of the resulting undulations of the pairs [IBW, IFW] and [IBW, OFW]. If the amplitude of the undulation built by [IBW, IFW] is observed to be larger than the one built by [IBW, OFW], then $IFW > OFW$ in terms of wave amplitude. Consequently, the relative importance of the above wave trains is: $IBW > IFW > OFW$. Similar reasoning will be applied below to Figures 5-7.

Reliable information based on steps 1-3 requires a dense cross-shore resolution over a minimal spatial domain. Therefore, in order to identify any node-antinode pattern whose mean distance between antinodes is L, the cross-shore resolution of the data set (Δx) must satisfy $\Delta x < L/2$. Note that $\Delta x \ll L/2$ is highly recommended when possible. Moreover, the spatial domain must include at least one node and one antinode, i.e., the distance between the first instrument (x_1) and the last instrument (x_{end}) of the experimental setup must satisfy $|x_{end} - x_1| \geq L/2$.

3. Quantitative analysis

3.1. The problem of wave separation

The wave separation method presented in this section is addressed in the frequency domain and applied over a number of cross-shore locations along changing water depths in the x-axis, i.e., $h = h(x)$. Therefore, at the target frequency f, the wave field η_f formed of n wave trains is

$$\eta_f(x,t) = \Re\left\{\left[\sum_{j=1}^{n} Z^j(x)\right] e^{-i(2\,\pi f t)}\right\} = \Re\left\{Z(x)\, e^{-i(2\,\pi f t)}\right\}, \qquad (17)$$

where $Z^j(x)$ is the cross-shore complex amplitude for each wave train j, whereas $Z(x)$ is the cross-shore measured complex amplitude by Fourier-transformation of the wave field $\eta_f(x,t)$. The wave separation method basically consists in obtaining $Z^j(x)$ for each wave train. As seen in Kostense (1985), Lin and Huang (2004) or Andersen et al. (2017), among many others, the typical separation method focuses on distributing the wave energy budget at the target frequency f among the n wave trains (e.g., IBW, OBW, IFW and OFW) based on their different propagation characteristics along a number P of wave gauges forming a local array. Within this local array, the wave separation at a reference gauge r (Z_r^j) is computed by solving the following linear system that involves local wave data measured at each gauge p (Z_p) (see Figure 4-a):

$$Z_p = \sum_{j=1}^{n} \left(Q_{r,p}^j \, Z_r^j \right) \quad \text{with } p \in \mathbb{R} : 1 \leq p \leq P, \tag{18}$$

where $Q_{r,p}^j = K_{r,p}^j \cdot e^{-i\Phi_{r,p}^j}$ represents the propagation coefficient of each wave train j travelling from the reference gauge r to each gauge p (subscript r,p). Consequently, K and Φ are factors that perform the cross-shore evolution of the amplitude and the phase, respectively, based on the nature of the wave train. These factors will be properly addressed below.

Note that the local array do not have to be formed of consecutive gauges, but different spatial resolutions for the wave separation (Δx_{sep}) may be defined as showed in Figure 4-b. The performance of the wave separation according to the spacing between the gauges forming the local array (controlled by the ratio $\Delta x_{sep}/\Delta x$) will be discussed below.

The wave separation method presented in this section can be applied to any frequency adapting the method to the number of existing wave trains and their propagation characteristics. Consequently, there is not a single definition of the separation method. In this paper, the proposed wave separation method accounts for the general combination: [IBW, OBW, IFW, OFW]. The

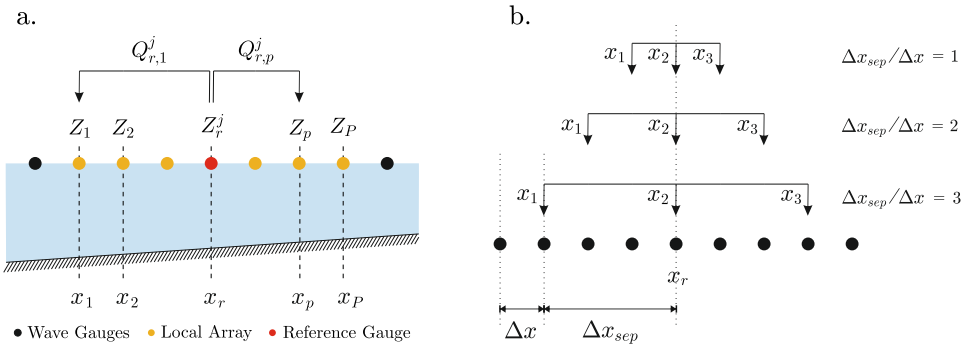

Figure 4: Plot a: Schematic layout of the wave separation method where Equation (18) is visually explained: the measured surface elevation at the wave gauge p, Z_p, is the sum of the wave trains at the reference gauge r, Z_r^j, propagated to the target gauge p by means of the propagation coefficient $Q_{r,p}^j$. Plot b: Example of a local array with $P = 3$ for $\Delta x_{sep}/\Delta x =$ 1, 2 and 3.

overdetermined version of the system presented in Equation (18) is

$$\begin{pmatrix} Q_{r,1}^{IBW} & Q_{r,1}^{OBW} & Q_{r,1}^{IFW} & Q_{r,1}^{OFW} \\ Q_{r,2}^{IBW} & Q_{r,2}^{OBW} & Q_{r,2}^{IFW} & Q_{r,2}^{OFW} \\ \vdots & \vdots & \vdots & \vdots \\ Q_{r,p}^{IBW} & Q_{r,p}^{OBW} & Q_{r,p}^{IFW} & Q_{r,p}^{OFW} \\ \vdots & \vdots & \vdots & \vdots \\ Q_{r,P}^{IBW} & Q_{r,P}^{OBW} & Q_{r,P}^{IFW} & Q_{r,P}^{OFW} \end{pmatrix} \begin{pmatrix} Z_r^{IBW} \\ Z_r^{OBW} \\ Z_r^{IFW} \\ Z_r^{OFW} \end{pmatrix} = \begin{pmatrix} Z_1 \\ Z_2 \\ \vdots \\ Z_p \\ \vdots \\ Z_P \end{pmatrix}. \tag{19}$$

For free waves (IFW and OFW), the wave celerity decreases as the water depth reduces following the Dispersion Equation. Therefore, the cross-shore amplitude evolves following the theoretical linear shoaling, i.e., the energy flux is preserved during cross-shore propagation. Consequently, the amplitude and phase propagation factors for j being the IFW and OFW are:

$$K_{r,p}^j = \left(\frac{c_{g,r}}{c_{g,p}}\right)^{1/2}, \tag{20}$$

$$\Phi_{r,p}^j = \int_{x_r}^{x_p} k(x)\,\cos(\theta^j(x))\,dx, \tag{21}$$

where c_g is the group celerity and $k(x)\,\cos(\theta^j(x))$ is the cross-shore component of the wave number vector.

The bound waves (IBW and OBW) require particular considerations. Their cross-shore amplitudes are assumed to follow a function of the local depth raised to a power α, e.g., $A^{IBW} \propto h^{-\alpha}$, as observed for subharmonic bound waves by Battjes et al. (2004) and Van Dongeren et al. (2007), among others. The celerities of the IBW and OBW (c^{IBW} and c^{OBW}) depend on the bound waves being superharmonics or subharmonics of the primary wave frequencies. For a superharmonic being the sum interaction of primary frequencies ($f_1 + f_1 = 2f_1$), the resulting superharmonic bound waves propagate with the celerity of the primary frequency, i.e., $c^{IBW} = c^{OBW} = c_{f_1}$. However for a subharmonic being the difference interaction of primary frequencies ($f_1 - f_2 = \Delta f$), the resulting subhamonic bound waves propagate with the group velocity of the mean primary frequency, i.e., $c^{IBW} = c^{OBW} = c_{g,f_p}$, where $f_p = (f_1 + f_2)/2$ (Janssen et al., 2003; Padilla and Alsina, 2017). As a result, the amplitude and phase propagation factors for j being the IBW and OBW are:

$$K^j_{r,p} = \left(\frac{h_r}{h_p}\right)^{\alpha^j}, \tag{22}$$

$$\Phi^j_{r,p} = 2\pi f \int_{x_r}^{x_p} \frac{1}{c^j(x)} \cos(\theta^j(x))\, dx. \tag{23}$$

The α-value is initially set to 1 for the IBW and OBW and after a first separation solving the Linear System (19), the resulting cross-shore amplitude of the IBW and OBW ($A^{IBW}(x)$ and $A^{OBW}(x)$) are immediately used to re-compute their α values, respectively. Using the function $A^j(x) = A^j_0\ (h_0/h(x))^{\alpha^j}$ as a good estimation of j being the IBW and OBW, α^j is the best fit parameter over the cross-shore bound wave amplitude in every iteration.

4. Results

4.1. Analysis of propagating wave trains

In this section, theoretical wave cases of wave trains with the same frequency but different propagation characteristics are analysed in Figures 5 - 7. These theoretical wave cases aim to reproduce the cross-shore behaviour of usual wave

trains at the primary frequency f_1 and its superharmonic $2f_1$. These wave trains are limited to one dimensional propagation (x-axis). For the wave trains propagating shoreward (IBW and IFW), the angle of incidence (θ) is 0. For the wave trains propagating seaward (OBW and OFW), $\theta = \pi$. Wave reflection is assumed to occur across the swash zone.

At the primary frequency f_1, the combination of wave trains is [IFW, OFW]. The resultant wave amplitude at f_1 is showed in Figure 5, where the undulation induced by the combination [IFW, OFW] is displayed. At the superharmonic $2f_1$, the combination of wave trains is [IBW, OFW]. The IBW propagates bound to the primary frequency f_1, whereas the OFW propagates seaward as a free wave. The resultant wave amplitude at $2f_1$ is showed in Figure 6, where the undulation induced by the combination [IBW, OFW] is displayed. Alternatively, the superharmonic $2f_1$ might be, under certain circumstances, the result of the combination of three wave trains: [IBW, IFW, OFW]. This situation is displayed in Figure 7. Note that although the same notation (OFW and IFW) is used for the free waves at the frequencies f_1 and $2f_1$, those are completely different wave trains. The notation OFW and IFW only accounts for their free nature and their propagation direction, regardless the target frequency.

For the theoretical examples displayed in Figures 5 - 7, the above type of wave trains (IBW, IFW and OFW) have been modelled in the following way:

$$IBW(x,t) = A_0^{IBW} \left(\frac{h_0}{h}\right)^{\alpha} \cos(2\pi f\, t - \widetilde{k}_x^{IBW} x + \psi_0^{IBW}), \quad (24)$$

$$IFW(x,t) = A_0^{IFW} \left(\frac{c_{g,0}}{c_{g,x}}\right)^{1/2} \cos(2\pi f\, t - \widetilde{k}_x^{IFW} x + \psi_0^{IFW}), \quad (25)$$

$$OFW(x,t) = A_0^{OFW} \left(\frac{c_{g,0}}{c_{g,x}}\right)^{1/2} \cos(2\pi f\, t - \widetilde{k}_x^{OFW} x + \psi_0^{OFW}), \quad (26)$$

where $f = f_1$ in Figure 5, whereas $f = 2f_1$ in Figures 6 and 7. Furthermore, [A_0^{IBW}, A_0^{IFW}, A_0^{OFW}] and [ψ_0^{IBW}, ψ_0^{IFW}, ψ_0^{OFW}] are the initial amplitudes and phases of the IBW, IFW and OFW, respectively. The used theoretical amplitudes and phases at x_0 ($x = 0$) for wave trains at f_1 and $2f_1$ in Figures 5 - 7 are displayed in Table 1. The used cross-shore bathymetry represents a 1:60

sloping bed, which is displayed in each figure. The used spatial resolution (Δx) is 0.05m.

Being $h = h(x)$, the average wave number $\widetilde{k}_x^j$ for each wave train j is computed as presented in Equation (11). For free waves at f_1, $\widetilde{k}_x^{IFW(f_1)}$ and $\widetilde{k}_x^{OFW(f_1)}$ are computed using the wave number given by dispersion relationship at f_1. For free waves at $2f_1$, $\widetilde{k}_x^{IFW(2f_1)}$ and $\widetilde{k}_x^{OFW(2f_1)}$ are computed using the wave number given by the dispersion relationship at $2f_1$. In contrast, the IBW at $2f_1$ travels bound to the primary frequency f_1 and, consequently, $\widetilde{k}_x^{IBW(2f_1)} = 2\,\widetilde{k}_x^{IFW(f_1)}$.

The cross-shore variation in amplitude of the free waves accounts for the cross-shore energy flux conservation. Therefore, the IFW and OFW evolve following linear shoaling with the coefficient $(c_{g,0}/c_g)^{1/2}$, where $c_g = c_g(x)$ is the group celerity. Conversely, the IBW amplitude growth during shoreward propagation follows a function of the local water depth raised to a power α, i.e., $A^{IBW} \propto h^{-\alpha}$. The IBW growth rate (α) used in Figures 6 and 7 is 0.9 (Table 1).

Table 1: Wave amplitudes and phases at x_0 ($x = 0$) of the IBW, IFW and OFW for the theoretical simulations in Figures 5 - 7. α is the IBW growth rate.

	Figure 5	Figure 6	Figure 7
	$f = f_1 = 0.45$Hz	$f = 2f_1 = 0.9$Hz	$f = 2f_1 = 0.9$Hz
A_0^{IBW} (m)	-	$1{\cdot}10^{-3}$	$1{\cdot}10^{-3}$
ψ_0^{IBW} (rad)	-	1.5	1.5
α	-	0.9	0.9
A_0^{IFW} (m)	$5{\cdot}10^{-3}$	-	$4{\cdot}10^{-4}$
ψ_0^{IFW} (rad)	2.7	-	5.7
A_0^{OFW} (m)	$3{\cdot}10^{-3}$	$6{\cdot}10^{-4}$	$6{\cdot}10^{-4}$
ψ_0^{OFW} (rad)	5.1	5.1	5.1

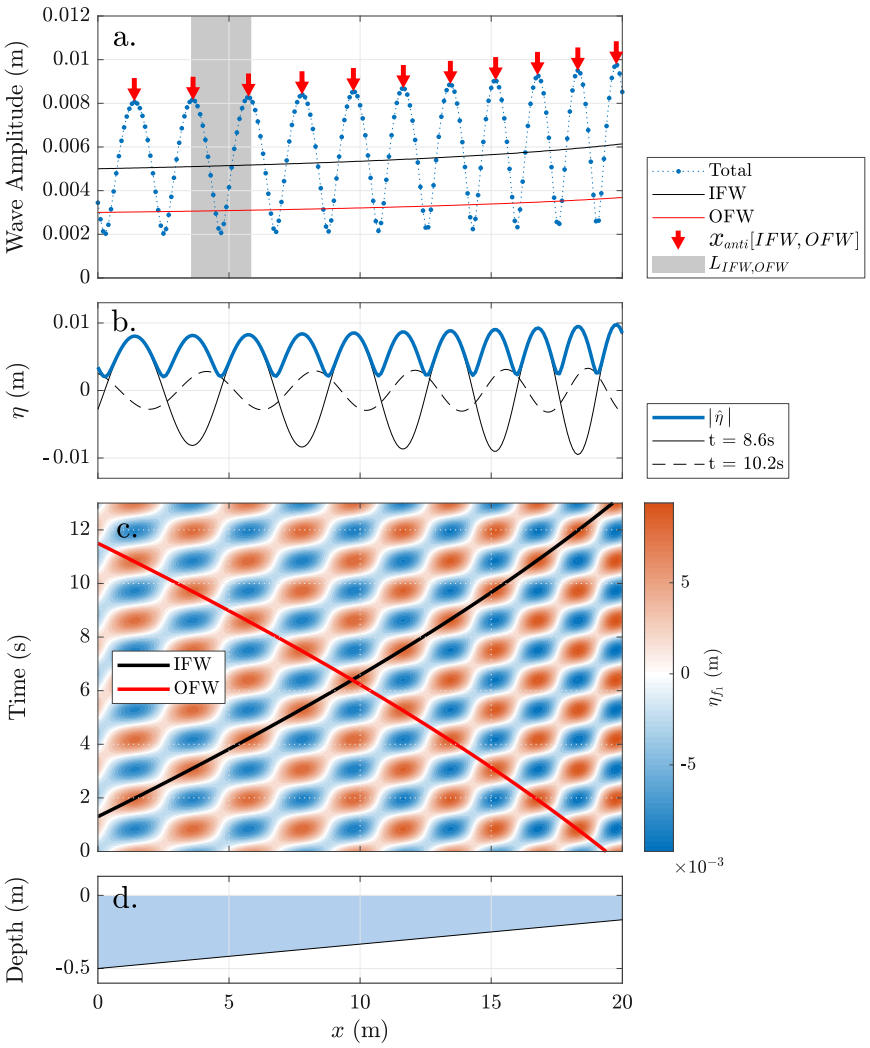

Figure 5: Theoretical propagation of two wave trains (IFW and OFW) at the primary frequency $f_1 = 0.45$Hz. Plot a shows the cross-shore evolution of the Total, IFW and OFW amplitudes (theoretical all of them). x_{anti} $[IFW, OFW]$ is the set of computed locations of the antinodes using Equation (13). $L_{IFW,OFW}$ (shaded area) is the flat-bed approximation of the mean distance between antinodes. Plot b shows the water surface elevation η_{f_1} at two different time instants alongside with its envelope. Plot c shows the η_{f_1} contour plot where the time-space trajectories of IFW and OFW are highlighted. Plot d illustrates the cross-shore water depth (1:60 sloping bed).

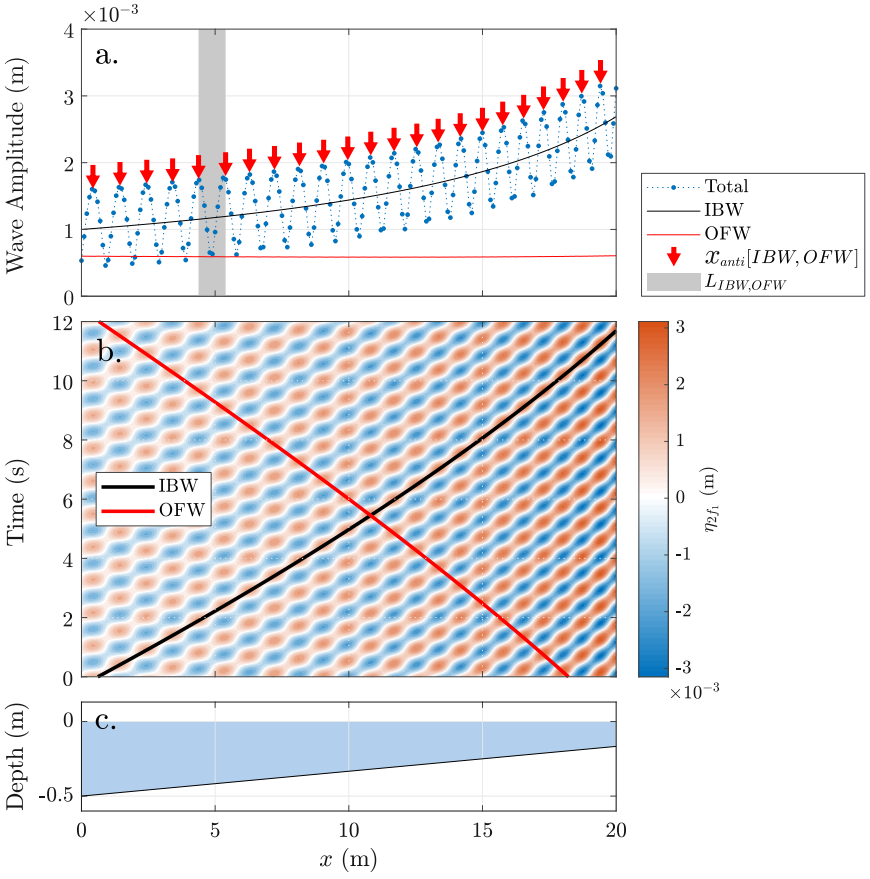

Figure 6: Theoretical propagation of two wave trains (IBW and OFW) at $2f_1 = 0.9$Hz. Plot a shows the cross-shore evolution of the Total, IBW and OFW wave amplitudes (theoretical all of them). x_{anti} [IBW, OFW] is the set of computed locations of the antinodes using Equation (13). $L_{IBW,OFW}$ (shaded area) is the flat-bed approximation of the mean distance between antinodes. Plot b shows the η_{2f_1} contour plot where the time-space trajectories of IBW and OFW are highlighted. Plot c illustrates the cross-shore water depth (1:60 sloping bed).

4.1.1. Case of two wave trains

Figure 5 presents the combination of the two wave trains [IFW, OFW] at the primary frequency $f_1 = 0.45$Hz. The IFW propagates shoreward, whereas the OFW travels seaward. The wave amplitude (blue line in plot *a*) and the envelope of the surface elevation $|\hat{\eta}|$ (blue line in plot *b*) display an undulating pattern resultant of the wave interaction of the pair [IFW, OFW]. As the water depth reduces, the wave amplitude grows (shoaling) and the distance between consecutive antinodes progressively decreases. As observed in Figure 5-*a*, the locations of these antinodes are in very good agreement with the estimation computed by Equation (13) marked with red arrows. Actually, $L_{IFW,OFW} = 2.3$m (shaded area in plot *a*) shows that Equation (10) may be a good a estimation of the average distance between the antinodes at the deepest end. For this wave case, the dominance of IFW over OFW, i.e., $A^{IFW} > A^{OFW}$ is seen in Figure 5-*c*. The time-space evolution of η_{f_1} highlights a dominant ingoing propagation in agreement with the time-space trajectory of the IFW.

Figure 6 presents the combination of the two wave trains [IBW, OFW] at $2f_1$ (0.9Hz). The incident wave train (IBW) travels bound to the primary frequency, whereas the OFW is a reflected wave train travelling seawards. In Figure 6-*a*, the wave amplitude (blue line) illustrates an undulating pattern resultant of the wave interaction of the pair [IBW, OFW]. The location of the antinodes is well determined by Equation (13) marked with red arrows, whereas the average distance between antinodes ($L_{IBW,OFW} = 1.01$m) is accurate using Equation (10). Furthermore, Figure 6-*a* also shows a progressive wave amplitude growth higher than the typical shoaling of free waves. In this case, the growth rate of IBW ($\alpha = 0.9$) is higher than the amplitude growth of OFW, i.e., the IBW dominates over the OFW. This dominance is also noticeable in Figure 6-*b*, where the time-space evolution of η_{2f_1} highlights a dominant ingoing propagation in agreement with the time-space trajectory of the IBW.

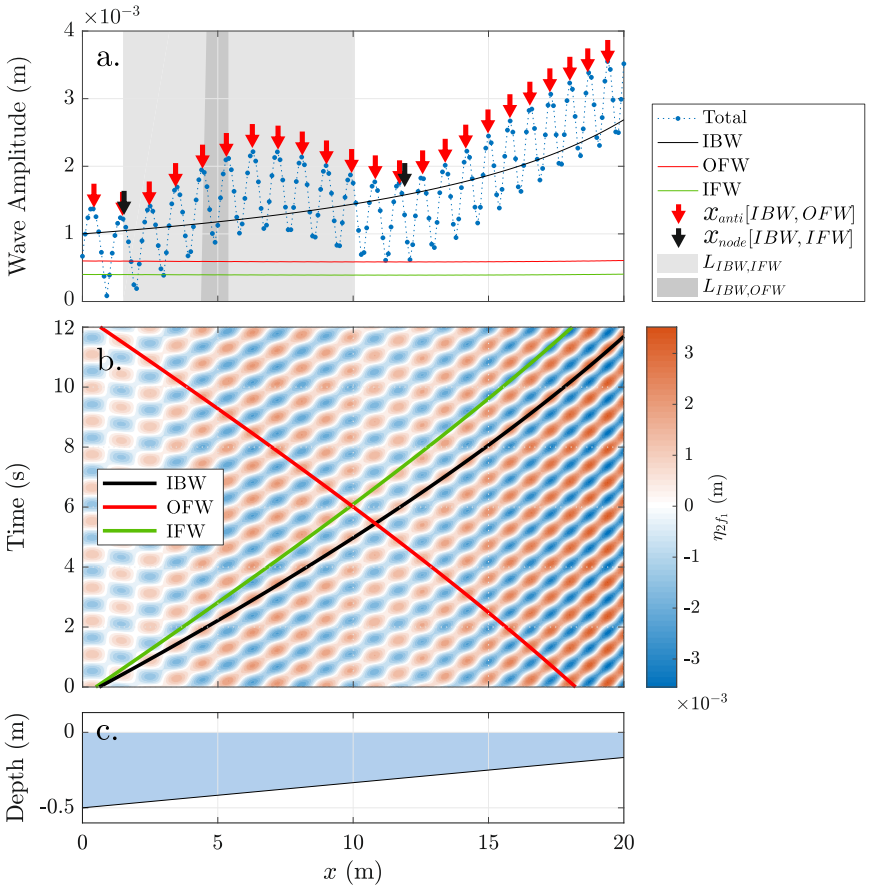

Figure 7: Theoretical propagation of three wave trains (IBW, IFW and OFW) at $2f_1 =$ 0.9Hz. Plot a shows the cross-shore evolution of the total and respective amplitudes (theoretical all of them). x_{anti} $[IBW, OFW]$ and x_{node} $[IBW, IFW]$ are the set of computed locations (using Equations (13) and (14), respectively) of the antinodes and nodes belonging the pairs $[IBW, OFW]$ and $[IBW, IFW]$, respectively. $L_{IBW,OFW}$ (light shaded area) is the flat-bed approximation of the mean distance between antinodes for $[IBW, OFW]$, whereas $L_{IBW,IFW}$ (light shaded area) applies for $[IBW, IFW]$. Plot b shows the η_{2f_1} contour plot where the time-space trajectories of IBW, IFW and OFW are highlighted. Plot c illustrates the cross-shore water depth (1:60 sloping bed).

4.1.2. Case of three wave trains

Figure 7 presents the combination of the three wave trains [IBW, IFW, OFW] at $2f_1$ (0.9Hz), which is an alternative situation to the one presented in Figure 6. The incident wave that travels bound to the primary wave (IBW) propagates shoreward alongside with an incident free wave (IFW). The remaining energy propagates seaward as a free wave (OFW).

In Figure 7-*a*, the cross-shore wave amplitude shows two clear undulating patterns and confirms the coexistence of at least three wave trains. The first undulating pattern involves the IBW and the OFW and is the one formed by antinodes marked in red arrows. The location of these antinodes (x_{anti} [IBW, OFW]) is estimated by Equation (13). Note that this undulating pattern has already been explained in Figure 6. The second undulating pattern involves the IBW and IFW and is the one formed by nodes marked in black arrows. The location of those nodes (x_{node} [IBW, IFW]) is successfully estimated by Equation (14).

The validity of Equation (10) over an sloping bed reduces with increasing distances, i.e., $L = \mathcal{O}(10)$m accumulates far more error than $L = \mathcal{O}(1)$m. For [IBW, OFW], the distance between consecutive antinodes progressively decreases as the water depth reduces, but $L_{IBW,OFW} = 1.01$m (darker shaded area in Figure 7-*a*) using Equation (10) is still a good approximation. For [IBW, IFW], the distance between consecutive nodes progressively increases as the water depth reduces. However, $L_{IBW,IFW} = 8.56$m (lighter shaded area in Figure 7-*a*) underestimates the real distance of 10.41m between the first and second node for the pair [IBW, IFW].

A third undulating pattern potentially develops associated to the pair [IFW, OFW]. The resultant average distance between consecutive nodes should be around $L_{IFW,OFW} = 0.91$m. However, this third pattern is not noticeable in Figure 7-*a* because the wave amplitudes of both IFW and OFW are far lower than the IBW amplitude. Therefore, this third undulating pattern is masked by the previous two undulating patterns. The dominance of IBW over IFW

and OFW is also confirmed by Figure 7-b, where the dominant propagation trajectory of η_{2f_1} is shoreward following the celerity of the IBW, i.e., the celerity of the primary frequency f_1.

4.2. Performance of the wave separation method

As described by the Linear System (19), the separation of the combination of wave trains [IBW, OBW, IFW, OFW] depends on the size of the local array (P), spatial resolution of the local array (Δx_{sep}) and the α-parameter (Equation (22)). Formally, a local array consisting of four different gauges ($P = 4$) is enough to solve the Linear System (19). However, the separation method may become numerically unstable and highly sensitive to noise if the phase difference across the gauges forming the local array is relatively small. Therefore, Battjes et al. (2004) suggest that a minimum array length is necessary to obtain a stable outcome when separating an experimentally measured wave field. Alternatively, the phase difference across the local array may be increased if Δx_{sep} increases, i.e., increase the distance between the solving gauges of the local array without increasing P (see Figure 4-b). Once P and Δx_{sep} are defined, the separation method is computed iteratively until convergence of the α-parameter.

In order to test the robustness of the wave separation method, Figure 8 illustrates the wave separation outcomes for the example case in Figure 7 with Gaussian White Noise (GWN) scaled to 1% of the wave height (see Appendix A). This wave separation in Figure 8 is accomplished using the following wave separation settings: [$P = 4$, $\Delta x_{sep} = 0.1$m] in plots a-b and [$P = 4$, $\Delta x_{sep} = 0.3$m] in plots c-d. When $P = 4$ and $\Delta x_{sep} = 0.1$m, the observed error in the separated wave trains is noise-dependent (Figure 8-a). When $P = 4$ and $\Delta x_{sep} = 0.3$m, the error associated to the added GWN is negligible in the separated wave trains as seen in Figure 8-c. Similar outcomes with negligible error are obtained when P increases to eleven, keeping $\Delta x_{sep} = 0.1$m (showed below in Figure 9). For the separation settings presented in Figure 8, α converged in no more than three iterations (plots b and d, respectively), although a far better estimation of α is obtained when the influence of noise

reduces.

Figure 9 illustrates the influence of P and Δx_{sep} on reducing the relative error associated to IBW, IFW and OFW for the example in Figure 7. The robustness of the wave separation method is also tested in Figure 9, where the separation is applied to the theoretical water surface elevation signal in Figure 7 with and without GWN (scaled to 1%). The relative error is computed as the Root-Mean-Square deviation:

$$RMSD\,(\%) = \frac{\sqrt{E[(A_{Th} - A_{Sp})^2]}}{A_{Th,0}} \cdot 100 \tag{27}$$

where $E[\cdot]$ denotes the expected value, and A_{Th} and A_{Sp} represent the cross-shore wave amplitudes of the Theoretical and Separated signals corresponding to IBW, IFW and OFW in each case.

A drastic decrease in the relative error is seen in Figure 9 when P increases from four to six for $\Delta x_{sep} = 0.1$m ($\Delta x_{sep}/\lambda \approx 0.055$). Similar error reduction is seen when Δx_{sep} increases from 0.1m to 0.15m (i.e., $\Delta x_{sep}/\lambda \approx 0.083$) for $P = 4$. Likewise, subsequent increases of P above eleven regardless $\Delta x_{sep}/\lambda$ or increases of Δx_{sep} above 0.3m ($\Delta x_{sep}/\lambda \approx 0.166$) regardless P do not really improve noticeably the wave separation outcomes. As expected, higher instability due to the noise is seen when P is low ($P = 4$). The effect of the noise is highly reduced when the number of solving gauges P increases from four to six, being practically suppressed when $P = 9$. Furthermore, the robustness of the separation method must be highlighted when no GWN is added (blue markers in Figure 9). In this case, the relative error is practically null for any wave separation setting considered.

5. Discussion

The separation of wave trains (ingoing, outgoing) for nonlinear and long waves is a fundamental task in many analyses of water surface time series. Different methods have been presented for linear incident waves over a plane bed (Goda and Suzuki, 1976; Mansard and Funke, 1980; Kostense, 1985; Frigaard

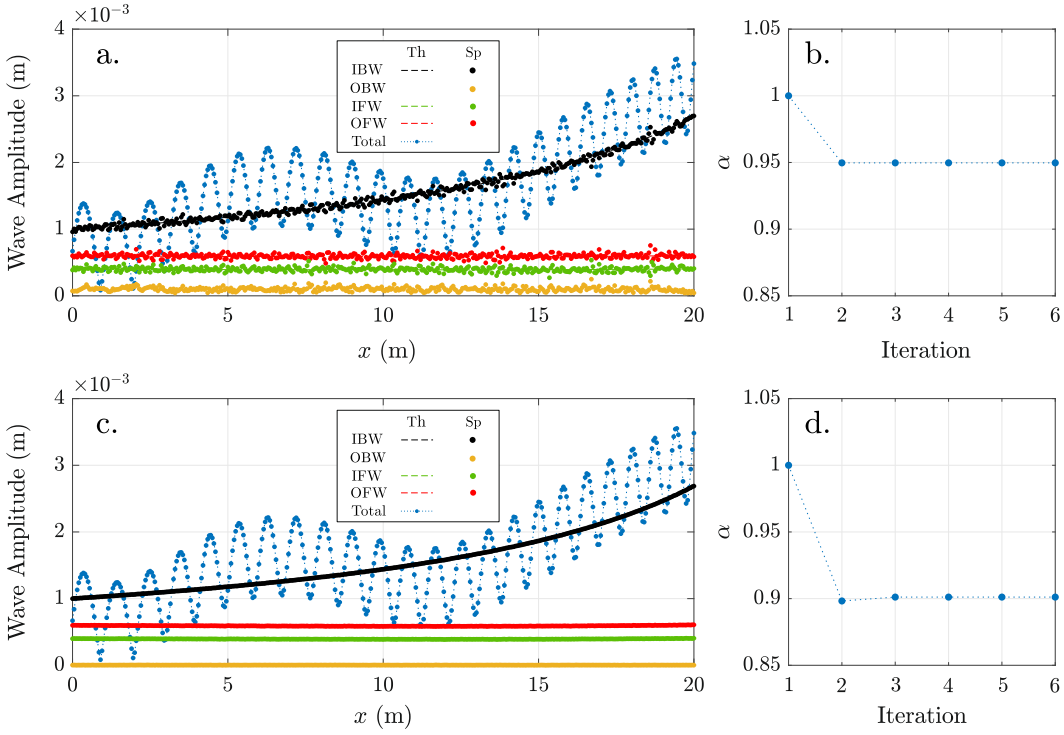

Figure 8: Separated wave trains of the example in Figure 7 with GWN ($\beta = 1\%$) under two different wave separation settings: [$P = 4$; $\Delta x_{sep} = 0.1$m] in plots *a*-*b*, and [$P = 4$; $\Delta x_{sep} = 0.3$m] in plots *c*-*d*. Plots *a* and *c* show the cross-shore wave amplitude evolution of the theoretical (Th) and the separated (Sp) wave trains, whereas plots *b* and *d* illustrate the convergence of the α-parameter associated to the IBW.

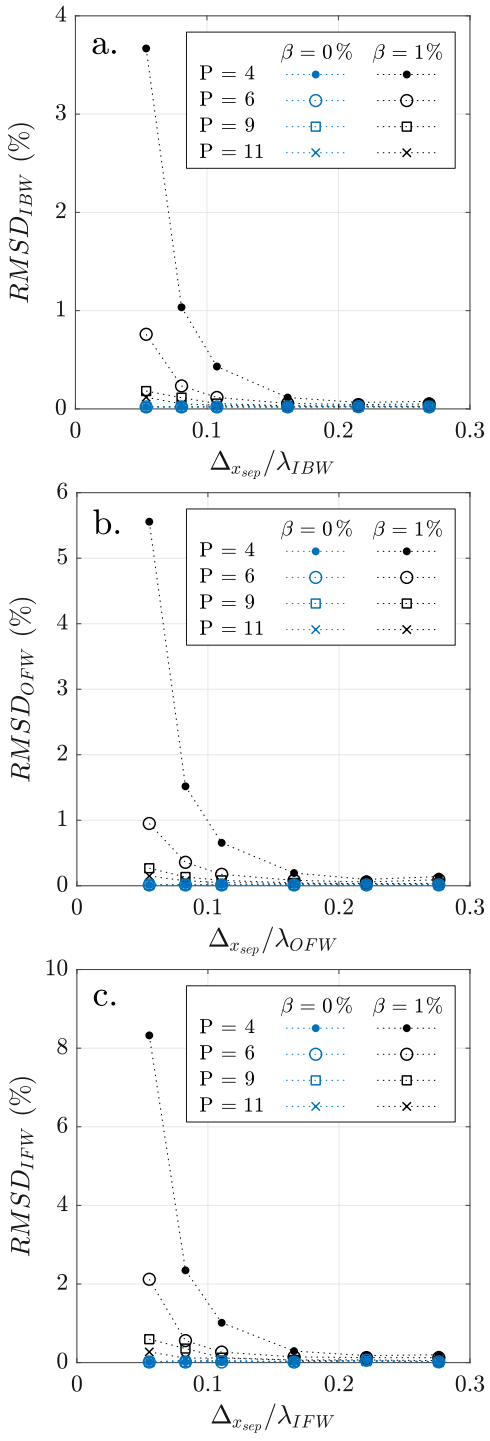

Figure 9: Relative error (RMSD) of the separated wave trains IBW (plot a), IFW (plot b) and OFW (plot c) for a range of wave separation settings involving P and Δx_{sep}. Time series of the example in Figure 7 with ($\beta = 1\%$; black) and without ($\beta = 0\%$; blue) GWN have been used.

and Brorsen, 1995), sloping bed (Baldock and Simmonds, 1999; Battjes et al., 2004; Van Dongeren et al., 2007), with some exceptions including wave nonlinearity (Lin and Huang, 2004; Andersen et al., 2017). Other presented methodologies (Battjes et al., 2004; Van Dongeren et al., 2007) consider long waves only. Existing methods generally use an array of wave gauges to compute the different wave trains either on the time or frequency domain. However, those methods require a previous knowledge of the existing wave trains and their nature, which is often assumed.

The qualitative analysis of the spatial undulating patterns of the cross-shore wave amplitude at the target frequency can provide very useful information about the number of existing wave trains, their nature (bound or free), propagation direction and relative importance. The qualitative analysis presented in section 2.3 and applied in Figures 5 - 7 is, in principle, applicable to any frequency (long or short waves) of field, numerical or experimental wave data when certain requirements about the spatial domain are fulfilled ($\Delta x \ll L/2$ and $|x_{end} - x_1| \geq L/2$).

In this paper, we have analysed the cross-shore behaviour of usual wave trains at the primary frequency f_1 and its superharmonic $2f_1$. However, no such analysis has been presented for low frequencies, like the difference interaction of primary frequencies ($\Delta f = f_1 - f_2$). The reason for not having presented the case of low frequencies is that no remarkable differences would be observed between, for example, Figure 6 and the corresponding figure to the pair [IBW, OFW] at Δf, but just a larger distance between consecutive nodes for Δf. The application of this general framework for wave separation at the subharmonics of experimental data has already been accomplished in Alsina et al. (2016), Padilla and Alsina (2017, 2018) and Ruffini et al. (2019).

The quantitative analysis presents a revisited wave separation method that allows the separation of ingoing and outgoing wave trains at any given frequency. This method is highly versatile because it accounts for the general combination of [IBW, OBW, IFW, OFW]. Therefore, this method is suitable for nonlinear waves and long waves propagating over beach-like environments. The separation

method assumes that superharmonics propagate with the velocity of primary frequencies, whereas subharmonics propagate with the group velocity associated to the primary frequencies. Although the information provided by the qualitative analysis is desirable, it is not fully essential. However, if the qualitative analysis suggests a more complicated combination of wave trains, then the linear system (19) should be accordingly modified.

If the qualitative analysis is carried out, the revealed information is a relatively good estimation of what the wave trains should look like. This estimation allows improvements in the separation outcomes by successive refinements of the wave separation settings, i.e., the number of wave gauges forming the local array (P) and their spatial resolution (Δx_{sep}). Although $P = 4$ is formally the minimum number of necessary wave gauges, a higher number has been traditionally used in order to minimise noise-related errors and guarantee the stability of the solution: five to nine gauges used by Battjes et al. (2004), ten gauges used by Lin and Huang (2004), seven gauges used by Van Dongeren et al. (2007) and five gauges used by Andersen et al. (2017). Note that the matrix $\mathbf{Q}^j_{r,p}$ in the Linear System (19) becomes singular when $\Delta x_{sep} \to 0$. Therefore, the separation problem is said to be ill-conditioned for low $\Delta x_{sep}/\lambda$ as observed in Figure 9 when $\Delta x_{sep} < 0.1$m. Conversely, the problem becomes well-conditioned for increasing values of $\Delta x_{sep}/\lambda$. No noticeable improvement is seen in Figure 9 for $\Delta x_{sep} > 0.3$. Therefore, a refinement of the spatial resolution with $\Delta x \leq 0.3$m for the example case in Figure 7 does not really offer any advantage from a wave separation perspective, but an increase in the computational cost (when numerically) or a cost excess in resources and time (when experimentally). On top of that, note that further singularity problems may arise when the resolution of the local array fulfils the following condition, introduced by Goda and Suzuki (1976) and confirmed by Lin and Huang (2004) (Equation 12c):

$$\frac{\Delta x_{sep}}{\lambda} = \frac{m}{2} \quad \text{with } m \in \mathbb{Z}, \tag{28}$$

which is not the case in this paper since $\Delta x_{sep}/\lambda \ll 0.5$. In order to propose an

operative threshold for the spatial resolution of the local array, Goda and Suzuki (1976) recommended that the ratio $\Delta x_{sep}/\lambda$ should be between 0.05 and 0.45, which is in agreement with the results in Figure 9. In general, a combination of relatively high $\Delta x_{sep}/\lambda$ (within the recommended threshold by Goda and Suzuki (1976)) and sufficient number of solving gauges ($P > 4$) should provide good results, but the optimal separation settings will depend on the target wave case.

This general framework for wave separation in the frequency domain is seen to be effective when the number n of wave trains at the target frequency is relatively low, i.e., $n \leq 4$. However, its application may become complicated when n increases, which is likely to happen for irregular waves. For irregular waves, there are multiple combinations of energetic frequencies whose nonlinear interaction give rise to the same frequency. At that frequency, n increases since there are many possible IBW trains, each of them travelling with its own velocity. For instance, each nonlinear interaction between frequency components [f_i, f_j] fulfilling $f_i - f_j = \Delta f$ would force a bound wave train IBW_{f_i,f_j} at the frequency Δf. Each IBW_{f_i,f_j} travels bound to its primary frequencies [f_i, f_j]. Therefore, a possible combination of wave trains at Δf (without considering any OBW) could be [IFW, OFW, IBW_{f_1,f_2}, IBW_{f_2,f_3}, ... , IBW_{f_i,f_j}], with $n > 4$. The superposition of this many wave trains builds a cross-shore wave amplitude where being able to identify the different undulating patterns will depend on the relative importance of those wave trains, i.e., their relative wave amplitudes. If the amplitudes of the bound wave trains are similar, identifying the different spatial undulating patterns at Δf will become very difficult ($N^* \ll N$ as mentioned in section 2.3) and the estimation of n using Equation (16) becomes very inaccurate. Consequently, any proposed version of the Linear system (19) built upon such a poor estimation of n results insufficient to properly separate the wave trains at Δf. If the amplitude of any of the bound wave trains dominates over the others (e.g., $IBW_{f_1,f_2} \gg IBW_{f_i,f_j}$), then the cross-shore wave amplitude at Δf presents a spatial undulating pattern that can be explained by few dominant wave trains. In this case, [IFW, OFW,

IBW_{f_1,f_2}, IBW_{f_2,f_3}, ... , IBW_{f_i,f_j}] can be reduced, in practical terms, to [IFW, OFW, IBW_{f_1,f_2}], n is three effectively and the framework for wave separation presented here can be applied. Irregular wave cases with n being low are relatively common as observed in Battjes et al. (2004) and Alsina and Cáceres (2011), where the power spectrum of irregular waves is divided in different frequency finite bands. Within each low frequency band, the cross-shore wave amplitude shows clear spatial undulating patterns (see Figure 5 in Alsina and Cáceres (2011)). Consequently, the framework for wave separation presented here could be successfully used to separate the dominant wave trains within each frequency band.

6. Conclusions

A general framework for wave separation in the frequency domain is presented to separate existing wave trains in the low and high frequency domain with satisfactory results. When a number n of wave trains travel with different propagation characteristics, their linear superposition results in a number N of different cross-shore undulating patterns formed of nodes and antinodes. However, the actual number n of existing wave trains is usually an uncertainty. The general framework for wave separation presented in this paper proposes a qualitative analysis to identify the number of existing wave trains, their nature (free or bound), their direction of propagation (ingoing or outgoing) and their relative importance. This analysis is based on the observation of the existing undulations (nodes-antinode patterns) forming the cross-shore wave amplitude structure at the target frequency and the observation of the main propagation trajectory of the surface elevation in the time-space domain.

The quantitative analysis of the framework is provided by a high versatile wave separation method that improves existing wave separation methods. Satisfactory results confirm its suitability to separate the general combination of wave trains: IBW, OBW, IFW and OFW, at any frequency (long or short waves) over uneven bathymetries. The robustness of the method is tested for a range of

wave separation settings [P, Δx_{sep}]. Satisfactory results are achieved when $0.1 < \Delta x_{sep}/\lambda < 0.3$ for a sufficient number of wave gauges ($P > 4$). The low sensitivity to noise of the method is tested using gaussian white noise over theoretical wave fields. A fully operative version of the separation method presented in this paper is available at GitHub (*https://github.com/EMPadilla/WaveSeparation.git*) alongside with the analysis and wave separation of the examples showed in this paper.

Appendix A. Gaussian white noise

Gaussian White Noise (GWN) was added to the water surface elevation to test the robustness of the wave separation method exactly in the same way as explained by Andersen et al. (2017). The noise signals are assumed spatially uncorrelated and calculated by the central limit theorem according to:

$$GWN(x,t) = \left(-\frac{N}{2} + \sum_{i=1}^{N} \xi_i \right) \sqrt{\frac{12}{N}}\, \beta\, H, \tag{A.1}$$

where ξ_i is a random number between 0 and 1, N is a sufficient large integer value, and β is the scaling factor of the noise, being 1% of the wave height H.

Acknowledgements

During this research, the first author was supported with a PhD fellowship from the Department of Civil and Environmental Engineering, Imperial College London. Codes underlying this article are available at GitHub: *https://github.com/EMPadilla/WaveSeparation* The authors thank the two reviewers for their suggestions, corrections and useful comments.

References

References

Alsina, J.M., Cáceres, I., 2011. Sediment suspension events in the inner surf and swash zone. measurements in large-scale and high-energy wave conditions. Coastal Engineering 58, 657–670.

Alsina, J.M., Padilla, E.M., Cáceres, I., 2016. Sediment transport and beach profile evolution induced by bi-chromatic wave groups with different group periods. Coastal Engineering 114, 325–340.

Andersen, T.L., Eldrup, M.R., Frigaard, P., 2017. Estimation of incident and reflected components in highly nonlinear regular waves. Coastal Engineering 119, 51–64.

Baldock, T., Huntley, D., Bird, P., O'Hare, T., Bullock, G., 2000. Breakpoint generated surf beat induced by bichromatic wave groups. Coastal Engineering 39, 213–242.

Baldock, T., Simmonds, D., 1999. Separation of incident and reflected waves over sloping bathymetry. Coastal Engineering 38, 167–176.

Baquerizo, A., 1995. Reflexión del oleaje en playas: Métodos de evaluación y de predicción. Ph.D. thesis. Universidad de Cantabria.

Baquerizo, A., Losada, M.A., Smith, J.M., Kobayashi, N., 1997. Cross-shore variation of wave reflection from beaches. Journal of waterway, port, coastal, and ocean engineering 123, 274–279.

Battjes, J., Bakkenes, H., Janssen, T., Van Dongeren, A., 2004. Shoaling of subharmonic gravity waves. Journal of Geophysical Research: Oceans 109.

Biésel, F., 1952. Équations générales au second ordre de la houle irrégulière. La Houille Blanche , 372–376.

Elgar, S., Herbers, T., Guza, R., 1994. Reflection of ocean surface gravity waves from a natural beach. Journal of Physical Oceanography 24, 1503–1511.

Frigaard, P., Brorsen, M., 1995. A time-domain method for separating incident and reflected irregular waves. Coastal Engineering 24, 205–215.

Goda, Y., Suzuki, T., 1976. Estimation of incident and reflected waves in random wave experiments. Coastal engineering proceedings 1.

Janssen, T., Battjes, J., Van Dongeren, A., 2003. Long waves induced by short-wave groups over a sloping bottom. Journal of Geophysical Research: Oceans 108.

Kostense, J.K., 1985. Measurements of surf beat and set-down beneath wave groups, in: Coastal Engineering 1984, pp. 724–740.

Lin, C.Y., Huang, C.J., 2004. Decomposition of incident and reflected higher harmonic waves using four wave gauges. Coastal engineering 51, 395–406.

Longuet-Higgins, M.S., Stewart, R., 1962. Radiation stress and mass transport in gravity waves, with application to 'surf beats'. Journal of Fluid Mechanics 13, 481–504.

Mansard, E.P., Funke, E., 1980. The measurement of incident and reflected spectra using a least squares method. Coastal Engineering Proceedings 1.

Padilla, E.M., Alsina, J.M., 2017. Transfer and dissipation of energy during wave group propagation on a gentle beach slope. Journal of Geophysical Research: Oceans 122, 6773–6794.

Padilla, E.M., Alsina, J.M., 2018. Long wave generation induced by differences in the wave-group structure. Journal of Geophysical Research: Oceans 123, 8921–8940.

Ruffini, G., Briganti, R., Alsina, J.M., Brocchini, M., Dodd, N., McCall, R., 2019. Numerical modeling of flow and bed evolution of bichromatic wave groups on an intermediate beach using nonhydrostatic xbeach. Journal of Waterway, Port, Coastal, and Ocean Engineering 146, 04019034.

Suh, K.D., Park, W.S., Park, B.S., 2001. Separation of incident and reflected waves in wave–current flumes. Coastal Engineering 43, 149–159.

Symonds, G., Huntley, D.A., Bowen, A.J., 1982. Two-dimensional surf beat: Long wave generation by a time-varying breakpoint. Journal of Geophysical Research: Oceans 87, 492–498.

Thornton, E.B., Calhoun, R.J., 1972. Spectral resolution of breakwater reflected waves. Journal of Waterways, Harbors & Coast Eng Div 98.

Van Dongeren, A., Battjes, J., Janssen, T., Van Noorloos, J., Steenhauer, K., Steenbergen, G., Reniers, A., 2007. Shoaling and shoreline dissipation of low-frequency waves. Journal of Geophysical Research: Oceans 112.

Zelt, J., Skjelbreia, J.E., 1993. Estimating incident and reflected wave fields using an arbitrary number of wave gauges, in: Coastal Engineering 1992, pp. 777–789.